



Research paper

Experimental analysis of resistance reduction and heel motion characteristics of wind-assisted vessels using the SIL system

Gyeongseo Min^a, Hyeongseok Yoon^a, Jaeyoon Jeon^a, Saishuai Dai^{b,***}, Sanghyun Kim^a,
Daejeong Kim^{c,**}, Seungnam Kim^d, Soonseok Song^{a,*}

^a Department of Naval Architecture & Ocean Engineering, Inha University, South Korea

^b Department of Naval Architecture, Ocean and Marine Engineering, University of Strathclyde, United Kingdom

^c Division of Navigation Convergence Studies, Korea Maritime & Ocean University, South Korea

^d Department of Naval Architecture and Ocean Engineering, Hongik University, South Korea

ARTICLE INFO

Keywords:

Software-in-the Loop (SIL)

Wind-Assisted Ship Propulsion (WASP)

Wing sail

ABSTRACT

In response to the recently strengthened regulations by the International Maritime Organization (IMO) concerning the Carbon Intensity Index (CII), there is a growing need to adopt alternative propulsion technologies to reduce fuel consumption and carbon emissions. In this context, wing sails, as one of the wind-assisted propulsion systems, are gaining attention as an eco-friendly solution to enhance ship fuel efficiency. However, their practical implementation requires a comprehensive assessment of their influence on ship stability under diverse sea conditions. To address this gap, this study experimentally evaluates the resistance reduction and roll motion characteristics of wing sail vessels under various marine environmental conditions using the Software-in-the Loop (SIL) method. In the present study, the SIL method creates a closed-loop system where the aerodynamic forces generated by wing sails are simulated as virtual forces and updated in real-time based on the measured motion of the vessel. As a result, the wing sail achieved a maximum resistance reduction of 33%, while the lateral force induced by the wing sail caused a maximum heel angle change of 0.6°. Furthermore, in terms of trim and sinkage, the wing sail showed a tendency to reduce trim, whereas sinkage remained unchanged.

1. Introduction

Maritime transportation accounts for the majority of global trade, while greenhouse gas emissions from ships constitute a large portion of total global greenhouse gas emissions. In response to climate change resulting from increased greenhouse gas emissions, the International Maritime Organization (IMO) adopted strategies for greenhouse gas reduction at the 80th session of the Marine Environment Protection Committee (MEPC). Specifically, these strategies target reductions of 20–30% by 2030 and 70–80% by 2040 relative to 2008 levels, with net-zero emissions by 2050 (IMO, 2023). Furthermore, since the introduction of the IMO greenhouse gas reduction strategies, the Carbon Intensity Indicator (CII) has been implemented to drive operational efficiency improvements and fuel reduction, with its methodology and review cycles being continuously refined.

In this context, Wind-Assisted Ship Propulsion (WASP) technologies

represent attractive solutions for reducing carbon emissions while enhancing operational efficiency in operations. These technologies encompass various systems, including wing sails, rotor sails, and kite systems (Chou et al., 2021; Guzelbulut and Suzuki, 2023; Li et al., 2020). Each system offers unique approaches to converting wind energy for vessel propulsion. Among these various wind-assisted ship propulsion technologies, wing sails have been regarded as well suited to commercial operations owing to their high lift-to-drag ratios, effective flow control, and suitability for automated trimming (Silva et al., 2019).

Recently, there were various previous studies on wing sail design and performance estimation. For example, a crescent-shaped profile for wing sails was developed to improve fuel consumption reduction efficiency (Zhu et al., 2023). This new profile was compared to the traditional airfoil section NACA 0015 through Computational Fluid Dynamics (CFD), and it was confirmed to have better efficiency. On the other hand, considering the ship's superstructure such as accommodation quarters,

* Corresponding author.

** Corresponding author.

*** Corresponding author.

E-mail addresses: saishuai.dai@strath.ac.uk (S. Dai), kdj4907@kmou.ac.kr (D. Kim), s.song@inha.ac.kr (S. Song).

the aerodynamic performance of the wing sail during actual operation was estimated through CFD under various angles of attack (AOA) and wind direction conditions. Furthermore, these results were compared with the standalone wing sail performance. Additionally, various experimental studies related to wing sails were conducted through wind tunnel tests from the perspectives of scale effects and performance evaluation (Fonseca and Soares, 2012; Wielgosz et al., 2025). Numerous studies have investigated the aerodynamic characteristics of wing sails. Commercial software such as Xfoil has been widely employed to analyze the lift and drag coefficients of airfoil sections used in wing sail design (Miller et al., 2018), enabling optimization of geometric parameters including chord length ratios (Kuang et al., 2023). These computational approaches provide valuable insight into wing sail performance under various operating conditions.

However, these experimental methods have the limitation of only considering the performance of the wing sail when it exists in isolation. This raises the question of whether there might be methods to simultaneously consider both the wing sail and the ship's motion in such performance evaluation experiments. Wing sails generate not only auxiliary propulsion but also lateral forces, which induce changes in ship motion. These motion changes alter the relative wind conditions and angles of attack experienced by the wing sail, thereby affecting its aerodynamic performance. The authors propose the Software-in-the Loop (SIL) methods as a solution to this question. The SIL method is an experimental approach that was used for Floating Offshore Wind Turbines (FOWT) (Arnal, 2020; Chen et al., 2021; Jiang, 2020). In this method, instead of installing and rotating an actual turbine in the experiment, the aerodynamic force generated by the turbine is replaced by a rotating fan that produces the corresponding forces. Specifically, the key point of this method is that as the FOWT moves, the aerodynamic force also changes accordingly, and this is reflected in real-time so that the force from the rotating fan varies in response to the floating body's motion.

There were previous studies that applied the SIL method to ships, similar to its application in FOWT, where ship motion analysis was conducted using a cable-driven robot to virtually represent sail forces (Sauder and Alterskjær, 2022). Furthermore, other research was conducted utilizing pulling fans to simulate the forces generated by wing sails while considering the ship's motion in real-time simulation (Werner et al., 2023). Both studies measured the forces generated by wing sails on cargo ships using the SIL method. However, the present study differs from these previous studies by conducting experiments on container ships, where heel motion poses significant risks due to potential container movement. Therefore, the aim of this study is to evaluate the influence of wing sails on the ship's heel motion through the SIL method under various wind speed and direction conditions. The influence was evaluated through 3-DOF towing carriage resistance experiments where heave, roll, and pitch motions were unconstrained. Moreover, two rotating fans were employed, with one simulating the auxiliary propulsive force that reduces resistance and the other replicating the lateral forces that wing sails exert on the ship's side.

This paper is organised as follows: The experimental set up and methodology of the present study are described in Section 2, which includes specific details on the geometry, SIL method, and uncertainty analysis for the present experiment. Section 3 presents roll, heave, and pitch motion variations in experiments and drag reduction under various wind conditions. Lastly, Section 4 summarized the present study results and discusses future research directions that can be developed using this approach, as well as the limitations of the current experiment.

2. Methodology

2.1. Experimental set up

2.1.1. Towing tank

The experiments were carried out at the Kelvin Hydrodynamics Laboratory (KHL) of the University of Strathclyde, utilizing a testing

facility measuring 76.0 m in length, 4.6 m in width, and 2.5 m in depth. The facility features advanced equipment including a computer-controlled carriage system capable of operating at speeds up to 5 m/s, and an advanced wave generating system with absorption capabilities. Specifically, Fig. 1 illustrated the towing carriage of the KHL. During the test, as depicted in Fig. 2, the model was free to heave, roll, and pitch. Trim and sinkage were estimated using two Linear Variable Differential Transducers (LVDTs) positioned at the midship and the bow. The trim angle was then calculated from the sinkage values at these two points using trigonometric relations. Roll motion was measured using an inclinometer, which was positioned at the same location as the Inertial Measurement Unit (IMU) equipment in the SIL system. The IMU's covariance parameters were adjusted to align with the inclinometer measurements, and the equivalence of readings from both sensors was verified during the experimental procedure. A load cell was installed at the tow point of the model ship to measure resistance forces during the experiments. Furthermore, fresh water was used as the testing medium during the experiments, with continuous water temperature monitoring to ensure consistent experimental conditions. Furthermore, as shown in Fig. 2, yaw guidance was employed to control yaw motion induced by lateral forces generated from the SIL system. The yaw guidance mechanism was positioned as close as possible to the free surface to prevent the suppression of roll motion. Additionally, all experiments were conducted at the ship's design speed condition.

2.1.2. Model ship towing test with SIL equipment

In this study, the KRISO Container Ship (KCS) was adopted for use in the experiments. The reason for selecting the KCS model is that roll motion can significantly affect containers loaded on container ship, making roll motion crucial for this vessel type. Specifically, the main particulars of the KCS were presented in Table 1. The model ship used in the experiments was scaled at a factor of 1:75 without rudder and appendages. Furthermore, the model ship experiments were conducted with three degrees of freedom, allowing the vessel to heave, roll, and pitch freely. However, as presented in Table 1, the present study set the metacentric height (GM) condition larger than the original KCS GM condition. The original GM of KCS ship is 0.008 m at the 75 scale used in the current research, but the present study was conducted with a GM of 0.059 m. This is because excessive roll motion caused by hull lateral forces generated through the SIL system could lead to green water risks, potentially damaging the equipment. Furthermore, the wing sail used in this study adopted a symmetric NACA 0015 section, as illustrated in Fig. 3. This airfoil was selected because it has been widely used in previous studies on wing sails (Hillenbrand et al., 2024; Ljungberg, 2023; Zhu, 2020). The wing sail dimensions were determined by linearly scaling a design originally developed for a 50K crude oil carrier with a length of 175m to the KCS hull with a length of 230m (Park et al., 2024). The chord and span lengths were adjusted proportionally. Specifically, the principal dimensions of the wing sail installed on the vessel were presented in Table 2.

The KCS model ship equipped with the SIL system was presented in Fig. 4. The rotating fan near the bow was designed to simulate the thrust generated by the wing sail during operation. This affected the force measured by the load cell. While the most accurate measurement method would be to directly influence the load cell, experimental limitations prevented direct connection to the load cell location. Therefore, the system was installed as described below. Furthermore, as shown in Fig. 4, the fan located at the stern of the model ship simulated the lateral force generated by the wing sail. Moreover, it was positioned close to the yaw guidance system to generate moments for roll motion while preventing unnecessary yaw motion.

2.2. SIL method

2.2.1. Equipment used in SIL system

The SIL system implemented in this study comprises an integrated

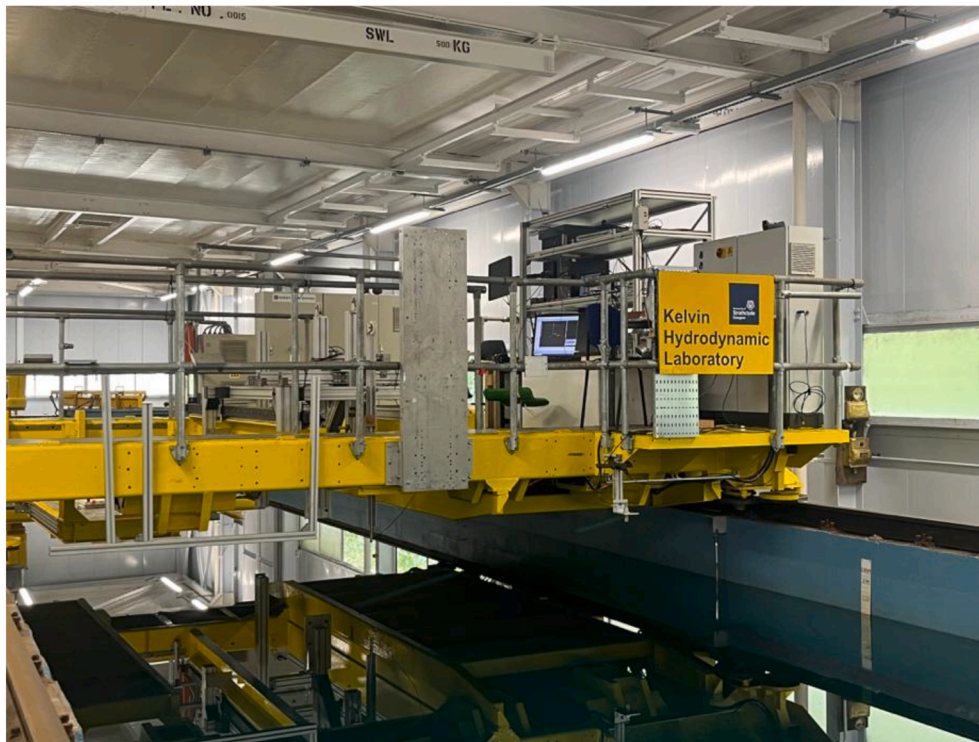


Fig. 1. Towing carriage of the Kelvin Hydrodynamics Laboratory, University of Strathclyde.

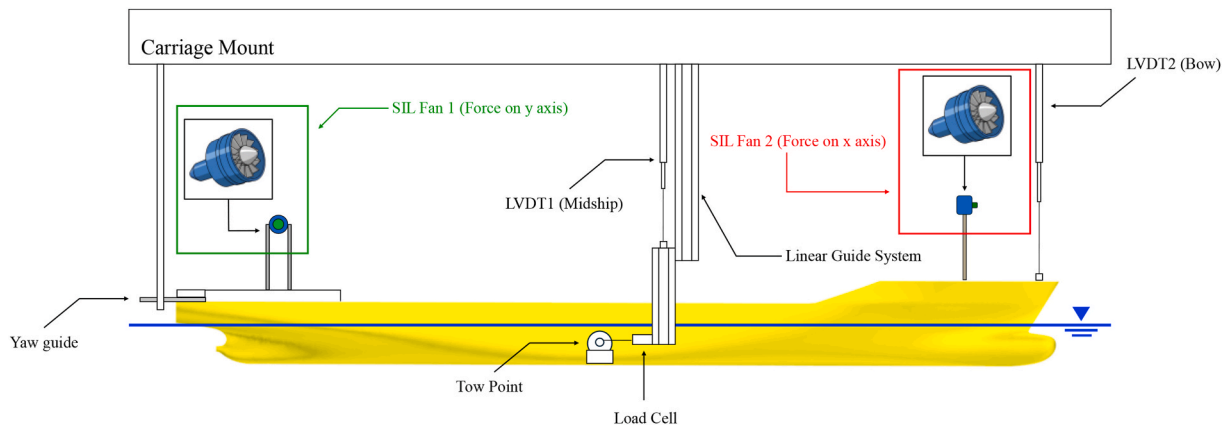


Fig. 2. Experimental setup with SIL system.

Table 1
Principal particulars of KCS.

Parameters		Full-scale	Model-scale
Scale factor	λ	1	75
Length between perpendiculars	L_{pp} (m)	230	3.0667
Beam at waterline	B_{wl} (m)	32.2	0.4293
Depth	D (m)	19.0	0.2533
Draft	T (m)	10.8	0.144
Wetted surface area without rudder	S (m^2)	9424	1.6754
Displacement	∇ (m^3)	52030	0.1233
Block coefficient	C_B	0.6505	0.6505
Design speed	V (knot, m/s)	24	1.426
Froude number	F_n	0.26	0.26
Metacentric height	GM (m)	0.6	0.059

hardware-software framework designed to replicate wing sail

aerodynamic effects on a model vessel in real-time. The architecture consists of three interconnected subsystems: a sensing unit that captures ship motions, a processing unit that performs aerodynamic calculations, and an actuation unit that generates physical forces. This arrangement creates a closed-loop control system wherein computed aerodynamic loads are physically applied to the model, while the vessel's motion response provides feedback for continuous force recalculation.

First, ship motion data was acquired through the myAHRS + Inertial Measurement Unit (IMU). The IMU continuously monitored the vessel's roll and pitch angles along with their respective angular velocities. This kinematic information enabled the numerical model to determine the instantaneous vessel state and compute relative wind conditions for aerodynamic force calculations. As the second component, the core computational element comprised a Raspberry Pi 4 single-board computer with 8 GB RAM that served as the central processing unit. The software architecture utilized ROS 2 (Robot Operating System 2) middleware to facilitate real-time inter-process communication between

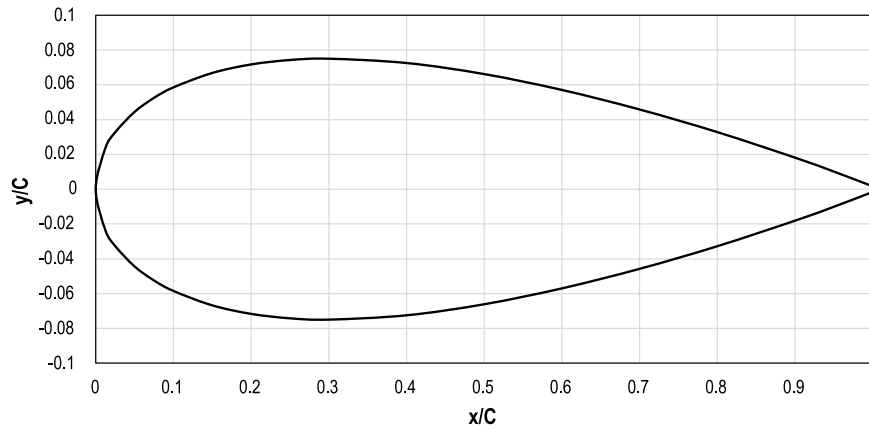


Fig. 3. Configuration of airfoil NACA 0015.

Table 2
Principal dimensions of wing sail.

Parameter		Full-scale	Model-scale
Scale	λ	1	75
Airfoil		NACA 0015	NACA 0015
Chord Length	c (m)	13.1429	0.1752
Span Length	b (m)	26.2857	0.3505
Projected area (m^2)	S (m^2)	345.4694	0.0614

distributed system components. Moreover, the computational workflow was divided into two primary modules: one executed the wing sail dynamics model implemented in Python, while the other converted computed forces into actuator control signals. Lastly, physical force generation was accomplished through two Lander 90 mm ducted fans, each equipped with a 1750W brushless DC motor. One fan generated longitudinal forces to simulate propulsive effects, while the other produced lateral forces to create roll moments on the vessel. Motor speed control was managed by dedicated Electronic Speed Controllers (ESCs), with an Arduino Mega 2560 microcontroller serving as the interface between the processing unit and the motor controllers. The overall hardware interconnection was illustrated in Fig. 5. The Arduino received thrust commands via USB serial communication and generates the corresponding PWM signals for motor operation. Furthermore, the complete hardware specifications were summarized in Table 3.

2.2.2. SIL system control algorithm

The wing sail load calculation and control allocation process followed the methodology presented in Fig. 6. The system computed

relative wind conditions from IMU measurements, derived aerodynamic forces through the wing sail model, and translated these forces into individual fan thrust commands. This process operated in a continuous control loop to maintain real-time system response. Specifically, the control algorithm operated in two distinct phases: First, it calculated the aerodynamic forces and moments from all wing sails considering the vessel's instantaneous motion state. Next, it allocated these total moments to individual fan thrust commands through geometric moment arm relationships. The detailed calculation methodology for this process was described below.

In determining the force calculation process for wing sails, the experimental conditions were established as follows. The coordinate system employed in this study was the body-fixed frame (Miller et al.) = $\{x_B, y_B, z_B\}$, where the positive directions of each axis were defined with the x-axis toward the bow, y-axis toward starboard, and z-axis upward. Furthermore, the wing sail was positioned at a fixed rotational angle of 30° (θ_c) about the z-axis relative to the body fixed reference frame. Four wing sails were incorporated into the experimental configuration, symmetrically positioned at offsets of $0.33L_{pp}$ in the x-direction and $0.04L_{pp}$ in the y-direction from the center of gravity, based on the full-scale KCS ship. In addition, considering container loading on deck, the wing sail span starting height was set as the equivalent of 5 container levels above deck, accounting for 4 stacked containers with 1 additional container height for clearance.

Under the aforementioned conditions, the relative velocity experienced by the wing sail was affected by the ship's motion as the towing tank advanced. This motion was detected by the IMU, and the dynamic relative wind velocity that accounts for the ship's movement was

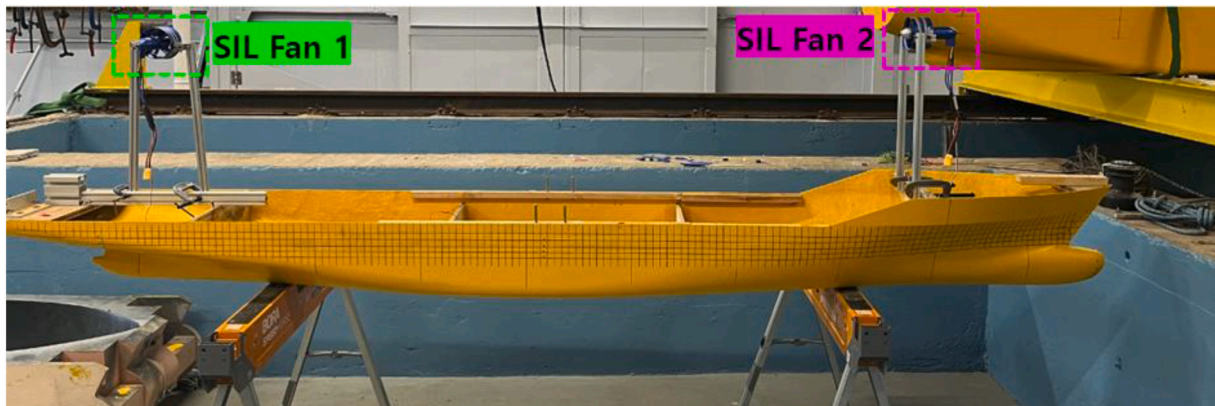


Fig. 4. KCS equipped with SIL system.

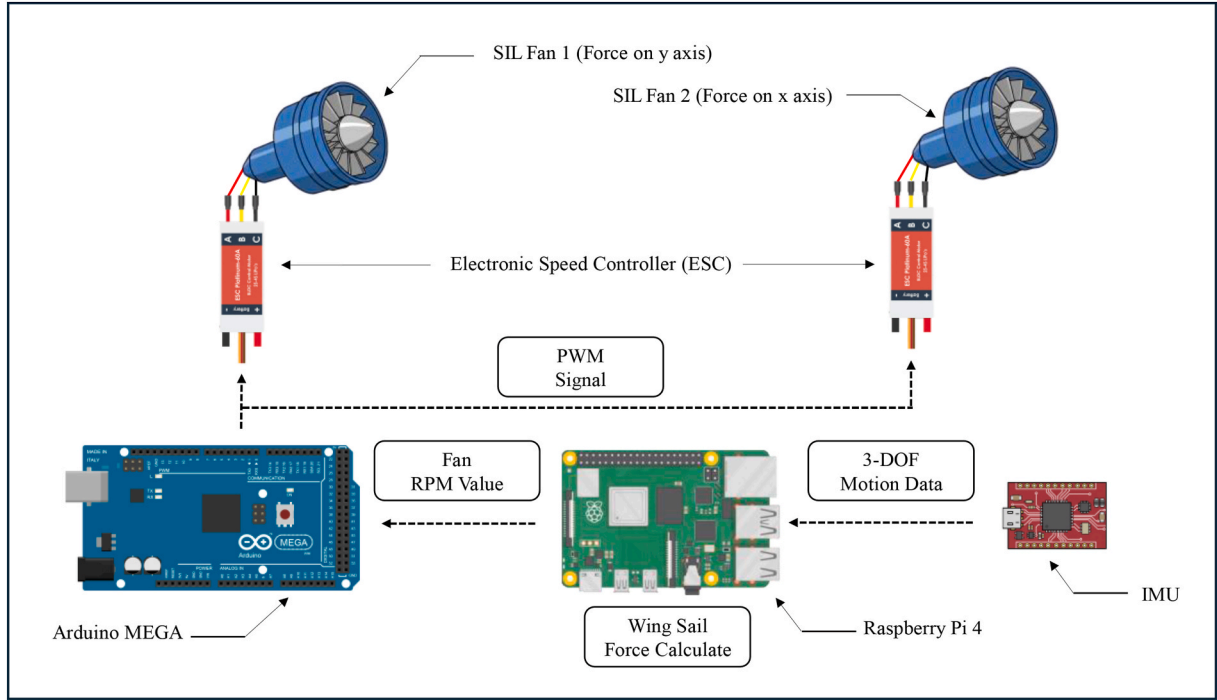


Fig. 5. Equipment used in the SIL system.

Table 3
SIL system hardware specifications.

Component	Specification	Function
Processing Unit	Raspberry Pi 4 Model B (8 GB RAM)	Real-time aerodynamic calculations
Sensing Unit	myAHRS + IMU	3-DOF motion measurement
Actuator	Lander 90 mm ducted fan (1750W) × 2	Physical force generation
Motor Controller	Electronic Speed Controller (ESC)	Brushless motor speed control
Interface	Arduino Mega 2560	PWM signal generation and communication

determined using Equation (1).

$$\vec{V}_{rel,i} = \vec{V}_{wind} - \vec{V}_{ship} - (\vec{\omega} \times \vec{r}_i) \quad (1)$$

where $\vec{r}_i = [x_i, y_i, z_i]^T$ denoted the position vector of the centroid of wing sails i , and $\vec{\omega} = [\omega_x, \omega_y, 0]^T$ was the ship's angular velocity vector, Here i represents the wing sail number ranging from 1 to 4. Moreover, \vec{V}_{wind} denoted the velocity vector of the wind, \vec{V}_{ship} denoted the velocity vector of the ship, and $\vec{V}_{rel,i}$ denoted the dynamic wind velocity vector of each wing sail. As a result, the 2-D component form was given in Equation (2) and Equation (3), with the magnitude is $V_{rel} = \|\vec{V}_{rel}\|$.

$$V_{rel,x} = V_{wind,x} - V_{ship,x} - \omega_y r_z \quad (2)$$

$$V_{rel,y} = V_{wind,y} - V_{ship,y} - \omega_x r_z \quad (3)$$

Then, using the equations described above, the dynamic relative wind velocity considering the ship's motion was derived, from which $\beta_i = \tan^{-1}\left(\frac{V_{rel,y}}{V_{rel,x}}\right)$ was obtained. As presented in Equation (4). The subtraction of the fixed installation angle (θ_c) yielded the dynamic relative angle of attack (α_{rel}).

$$\alpha_i = \beta_i - \theta_c \quad (4)$$

Furthermore, the configuration of the dynamic relative angle of attack was illustrated in Fig. 7.

Next, the process of calculating the lift and drag forces using the dynamic relative angle of attack derived from Fig. 7 was described. The lift and drag coefficients were obtained using a commercial program Xfoil, and all calculations were performed at Reynolds numbers corresponding to each wind speed. Specifically, These coefficients were evaluated at the full-scale Reynolds number using Xfoil to achieve Reynolds similarity, rather than at the model-scale Reynolds number. Furthermore, the reason for selecting the Xfoil program to calculate lift and drag forces is that the wing sail has a relatively simple geometry with a constant cross-section and chord length. Therefore, the potential flow-based Xfoil program was chosen to perform these calculations with low computational cost. As a result, the C_L and C_D curves as functions of the angle of attack were obtained, as shown in Fig. 8. Additionally, these were used in the experiment through polynomial approximation. When the lift and drag coefficients associated with the dynamic relative angle of attack were obtained, these coefficients enabled the computation of auxiliary thrust and transverse forces acting on the ship in the body-fixed coordinate system, as expressed in Equations (5) and (6).

$$C_{x,i} = -C_D \cos \beta_i - C_L \sin \beta_i \quad (5)$$

$$C_{y,i} = -C_D \sin \beta_i - C_L \cos \beta_i \quad (6)$$

Under the uniform inflow assumption, the corresponding full-scale force components acting on the ship were given by Equations (7) and (8), where S denoted the projected area of the wing sail.

$$F_{x,i}^{full} = C_{x,i} \frac{1}{2} \rho_{air} S^{full} \|V_{rel,i}^{full}\|^2 \quad (7)$$

$$F_{y,i}^{full} = C_{y,i} \frac{1}{2} \rho_{air} S \|V_{rel,i}^{full}\|^2 \quad (8)$$

The model-scale wind speed $\|V_{rel,i}^{model}\|$ was determined by applying Froude scaling to the full-scale wind speed:

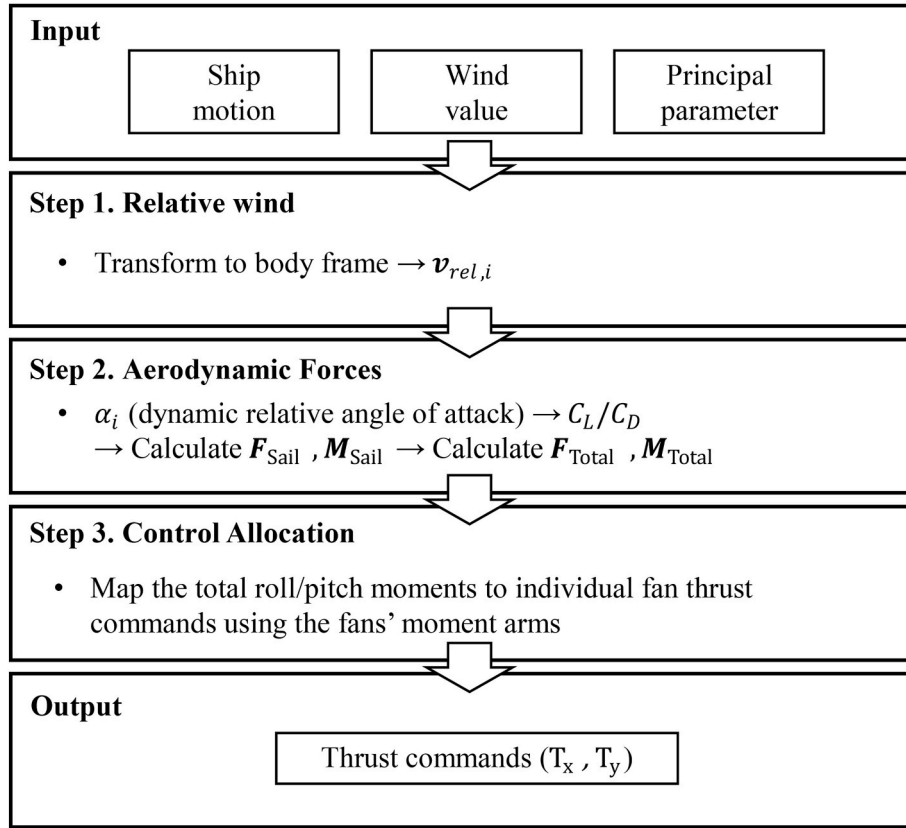


Fig. 6. Algorithm for the SIL system.

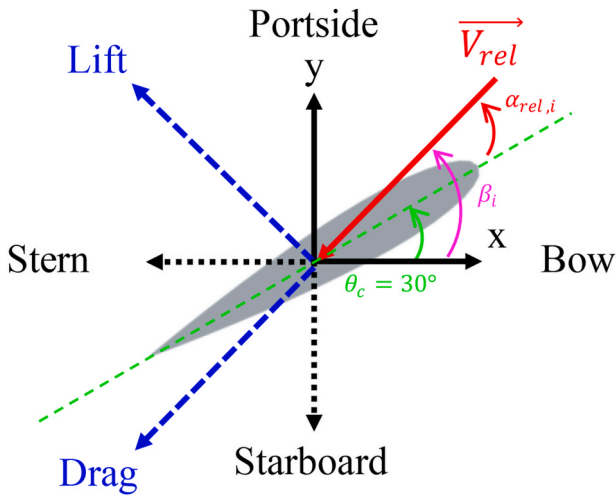


Fig. 7. Configuration of relative angle of attack.

$$\|V_{rel,i}^{model}\| = \frac{\|V_{rel,i}^{full}\|}{\sqrt{\lambda}} \quad (9)$$

where λ denotes the scale ratio of the model ship. This is consistent with the Froude-scaled towing speed and ensures that the ratio of aerodynamic to hydrodynamic forces is preserved between model and full scale. Substituting the Froude scaling relations for projected area ($S^{model} = S^{full}/\lambda^2$) and wind speed (Equation (9)) into Equations (7) and (8):

$$F_{x,i}^{full} = C_{x,i} \cdot \frac{1}{2} \cdot \rho_{air} (\lambda^2 S^{model}) (\sqrt{\lambda} \|V_{rel,i}^{model}\|)^2 = \lambda^3 \cdot C_{x,i} \cdot \frac{1}{2} \cdot \rho_{air} S^{model} \|V_{rel,i}^{model}\|^2 \quad (10)$$

Therefore, the model-scale aerodynamic forces can be expressed directly as:

$$F_{x,i}^{model} = C_{x,i} \cdot \frac{1}{2} \cdot \rho_{air} S^{model} \|V_{rel,i}^{model}\|^2 \quad (11)$$

$$F_{y,i}^{model} = C_{y,i} \cdot \frac{1}{2} \cdot \rho_{air} S^{model} \|V_{rel,i}^{model}\|^2 \quad (12)$$

This formulation show that when the model-scale projected area S^{model} and Froude-scaled wind speed $\|V_{rel,i}^{model}\|$ are used directly, the model-scale forces are obtained without an additional scaling step. The coefficients C_L and C_D , and hence $C_{x,i}$ and $C_{y,i}$, remain identical between full scale and model scale, as they are evaluated at the full-scale Reynolds number, thereby satisfying Reynolds similarity.

Finally, the moments acting along the x-axis and y-axis that influence the ship's motion were estimated, and the total moment required in each axial direction was determined by summing all corresponding moments for axis. This process can be verified through Equations (13)–(15), where h_i^{model} represented the position of the wing sail's center of height at model scale.

$$M_{x,i}^{model} = F_{y,i}^{model} h_i^{model} \quad (13)$$

$$M_{y,i}^{model} = F_{x,i}^{model} h_i^{model} \quad (14)$$

$$\vec{M}^{model} = \sum_i [M_{x,i}, M_{y,i}]^T \quad (15)$$

in this study fans were installed 50 cm above the model ship's deck.

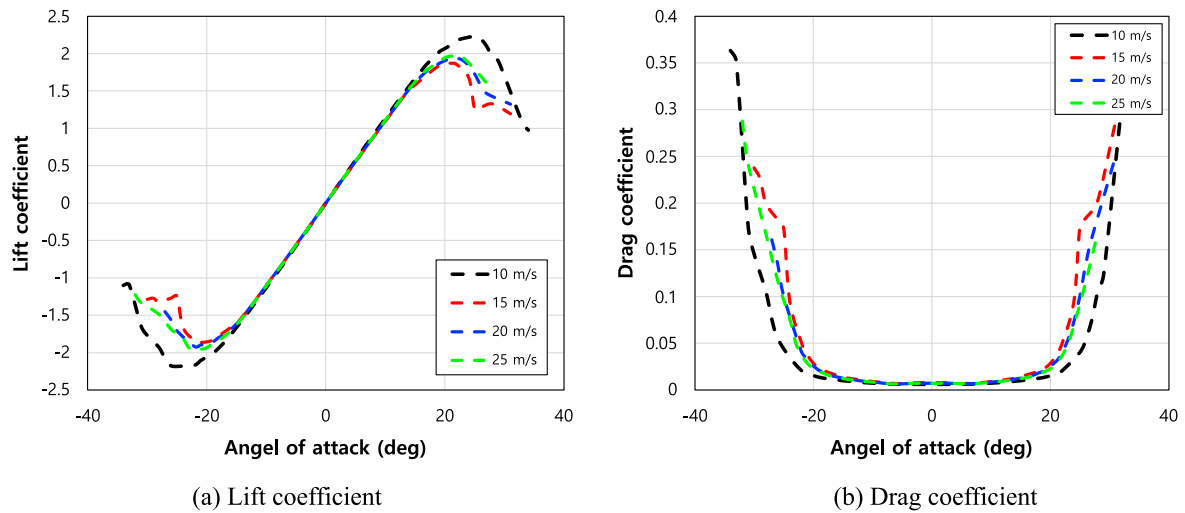


Fig. 8. Lift and drag coefficients curves obtained by Xfoil.

Based on this experimental setting, the required fan forces in each axial direction were derived as shown in Figs. 3 and 4. The corresponding fan rpm values were determined using data obtained through fan calibration, and these values were transmitted as control signals. This real-time computational loop process performed during the experiment constituted the SIL methodology employed in this study. In this scaling process, the hydrodynamic forces followed Froude scaling through the towing speed, while the aerodynamic forces satisfied Reynolds similarity through the lift and drag coefficients based on full-scale Reynolds numbers. The model-scale wind speed was then adjusted following Froude scaling to maintain the correct ratio between aerodynamic and hydrodynamic forces.

2.3. Uncertainty analysis

Uncertainty analysis for the experiments was conducted by dividing it into two parts. One case as the condition without the SIL system, and the other was the case with the SIL system. Additionally, for the case with the SIL system, the analysis was performed separately for the highest and lowest wind speed conditions. All of these were conducted according to ITTC recommended procedures (ITTC, 2014). Furthermore, precision limits were determined through repeated experiments under identical conditions, while bias limits were measured according to the experimental conditions of this study for calibration, data acquisition, data reduction, and conceptual bias. Specifically, Table 4 presents the

Table 4 Overall uncertainty analysis for experiments.

Without SIL system	Overall uncertainty	%
B_{Rr} (N)	3.736E-2	5.371E-1
B_p (kg/m ³)	1.984E-2	1.987E-3
B_S (m ²)	1.082E-2	6.458E-1
B_V (m/s)	1.000E-3	7.012E-2
B_{Cr}	3.482E-5	8.512E-1
P_{Cr}	2.058E-5	5.033E-1
U_{Cr}	4.045E-5	9.891E-1
SIL system (10 m/s)	Overall uncertainty	%
B_{Cr}	3.482E-5	8.512E-1
P_{Cr}	9.551E-5	2.841E-0
U_{Cr}	1.002E-4	2.981E-0
SIL system (30 m/s)	Overall uncertainty	%
B_{Cr}	3.482E-5	8.512E-1
P_{Cr}	7.659E-5	2.801E-0
U_{Cr}	8.118E-5	2.970E-0

results of the overall uncertainty analysis for the present study. As mentioned previously, the initial uncertainty analysis for experiments conducted without the SIL system showed approximately 0.99%, which is below 1%. However, the experiments using the SIL system under both the highest and lowest wind speed conditions showed approximately 2.98%, indicating an increased uncertainty compared to the results without SIL conditions. These results were attributed to the uncertainty associated with the fan used in the experiments, likely due to the diffusion effects of the rotating wind. But, since the primary focus of this study was on applying the SIL methodology to towing tank experiments, the use of fans was necessary for implementing the real-time closed-looped system, making this uncertainty inevitable. Moreover, in the case of experiments using the SIL system, it was difficult to derive uncertainty through direct bias limits related to the fan. Therefore, the uncertainty was measured by incorporating it through precision limits.

3. Results

In this section, the experimental results were discussed for various wind speeds and selected wind angles, focusing on the resistance and motions (heel, trim, and sinkage) of the KCS model equipped with a wing sail. All tests were performed at a constant Froude number ($F_n = 0.26$), corresponding to a model speed of 1.426 m/s (12.346 m/s at full scale). Specifically, the detailed test conditions were summarized in Table 5 and Fig. 9. The experiments were conducted at four wind angles: 50°, 45°, 30°, and 20°. Considering the wing sail was fixed at 30° relative to the ship's centerline, the initial angles of attack were 20°, 15°, 0°, and 10° respectively. Notably, the case with a wind angle of 20° differs from the other three cases in that the direction of the lateral force on the ship is reversed. Furthermore, all test cases were validated through repeated experiments to ensure reproducible results, and all wind speed conditions presented in Table 5 correspond to full-scale values.

Table 5 Test cases at specified relative angle of attack and wind speeds.

Test cases	Wind speed	10 m/s	15 m/s	20 m/s	25 m/s
Wind angle 50°		Case 1.1	Case 1.2	Case 1.3	Case 1.4
Wind angle 45°		Case 2.1	Case 2.2	Case 2.3	Case 2.4
Wind angle 30°		Case 3.1	Case 3.2	Case 3.3	Case 3.4
Wind angle 20°		Case 4.1	Case 4.2	Case 4.3	Case 4.4

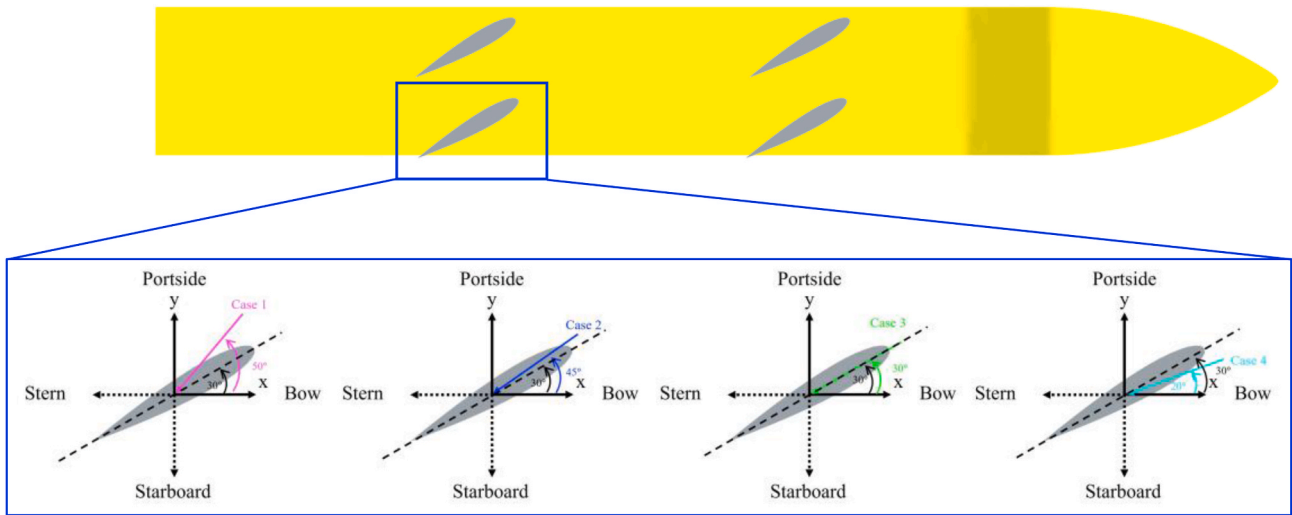


Fig. 9. Configuration of each case according to wind angle.

3.1. Drag reduction effect by the wing sail

The results of drag measured through the experiments were depicted in Fig. 10. As shown in Fig. 10, the drag of the ship equipped with a wing sail was consistently lower than that without a wing sail. To examine the effect of wind speed, cases with a fixed wind angle were first investigated. In all four wind angle conditions, resistance consistently decreased as wind speed increased. Similarly, under identical wind speed conditions, as increasing trend in resistance reduction rate was observed as the initial relative angle of attack increased. Furthermore, the reduction rate of drag related to the without wing sail condition was depicted in Fig. 11. The drag reduction rated across all cases varied from 9.26% to 33.23%. Moreover, these quantitative results of drag reduction rates for all cases were presented in Table 6. The increase in drag reduction rate with higher wind speeds was primarily attributable to the corresponding increase in absolute lift force magnitude. As wind speed increases, the generated lift force becomes larger, resulting in greater propulsive thrust and enhanced resistance reduction. At a constant wind speed, variations in wind direction altered the initial angle of attack, thereby changing the lift and drag coefficients. The resulting increase in lift force with larger angles of attack was the primary mechanism responsible for the observed drag reduction characteristics.

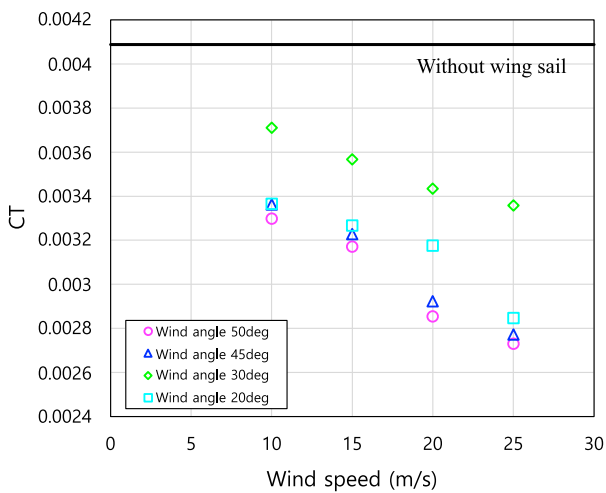


Fig. 10. Resistance variation of wing sail equipped vessel under various wind conditions.

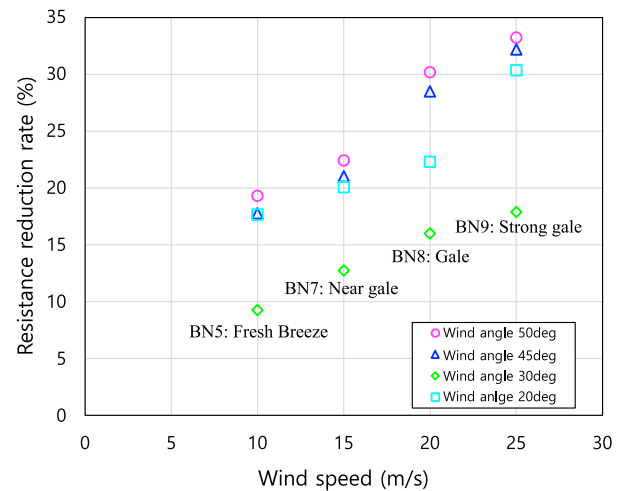


Fig. 11. Drag reduction rate achieved by wing sail across various wind conditions.

Table 6
Quantitative estimation of resistance reduction rate under various wind conditions.

Resistance reduction rate	Wind angle				
	20°	30°	45°	50°	
Wind speed	10 m/s	17.67%	9.26%	17.77%	19.32%
	15 m/s	20.08%	12.74%	21.03%	22.44%
	20 m/s	22.31%	16.00%	28.51%	30.19%
	25 m/s	30.36%	17.89%	32.18%	33.23%

The observed trend of increasing drag reduction rates with higher wind speeds appears to indicate that stronger winds are always beneficial for wing sail operation. However, the 25 m/s wind speed condition that exhibited the highest drag reduction rate corresponds to Beaufort number 9, classified as a strong gale. In this context, considering that wing sails also generate lateral forces on the ship, a question arises regarding whether it is safe to operate wing sails under such severe weather conditions. From this perspective, the variations in heel motion were subsequently analyzed in Section 3.2.

3.2. Results of heel variation

The heel variation due to the wing sail were illustrated in Fig. 12. Before describing the heel angle variation, it should be noted that a positive heel angle indicates tilting toward the starboard side, while a negative heel angle indicates tilting toward the portside. As shown in Fig. 12, heel angles increased significantly with both increasing wind speed and increasing initial relative angle of attack of the wing sail. These results were consistent with the drag trends observed in Section 3.1. Furthermore, these results were quantitatively presented in Table 7. As indicated in Table 7, the heel angle exhibited increases ranging from 0.27 to 0.6°. These results follow the same principles discussed in Section 3.1. At a constant initial angle of attack, as the absolute wind speed increases, both the lift force contributing to drag reduction and the drag force increase proportionally, and this simultaneous increase in aerodynamic forces lead to a corresponding increase in later force induced primarily by the drag component, which in turn results in greater heel angle. Similarly, at constant wind speed, the increase in heel angle with larger initial angles of attack results from concurrent increases in both lift and drag forces, which generate greater lateral loads and induce larger heel angles.

However, readers may consider these differences to be negligible due to their small absolute values. Nevertheless, it should be noted that the heel angle was zero under windless conditions, and as previously mentioned, the current experimental setup utilized a GM value significantly larger than that of the actual KCS due to experimental equipment constraints. Considering these factors, the observed heel variations can be regarded as substantial. Furthermore, future investigations conducted under actual GM of KCS ship conditions are expected to yield more pronounced results.

Therefore, these results demonstrate that wing sails may adversely affect ship stability of roll motion under high wind speed conditions and depending on the wing sail angle of attack. Such increases in heel angle can result in significant motion variations for container ships, depending on container loading conditions, suggesting that this factor should be carefully considered when implementing wing sails on container ships.

3.3. Results of trim and sinkage variations

In this part, the results of trim and sinkage variation in wing sail equipped vessels across wind speeds and relative angles of attack were presented. Before explaining the results, it should be noted that negative trim value in this paper indicates a condition where the ship is trimmed down by the bow. As shown in Fig. 13, the trim decreased as wind speed

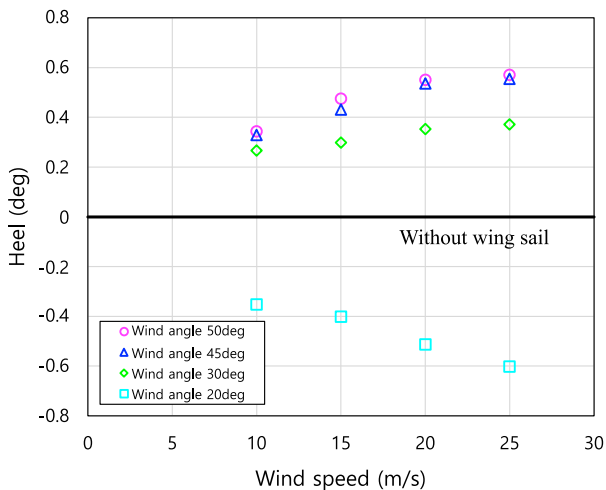


Fig. 12. Heel variation under various wind conditions.

Table 7

Quantitative estimation of heel variation under various wind conditions.

Heel variation		Wind angle			
		20°	30°	45°	50°
Wind speed	10 m/s	-0.35 °	0.27 °	0.33 °	0.34 °
	15 m/s	-0.40 °	0.30 °	0.43 °	0.48 °
	20 m/s	-0.51 °	0.35 °	0.54 °	0.55 °
	25 m/s	-0.60 °	0.37 °	0.56 °	0.57 °

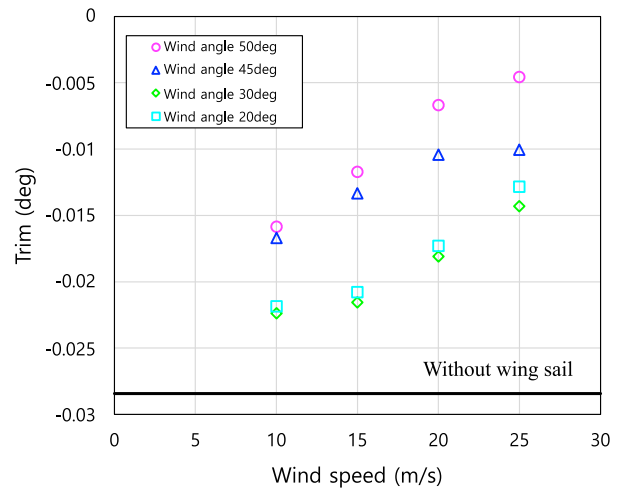


Fig. 13. Variation of trim under various wind conditions.

increased at a fixed relative angle of attack. Similarly, increasing the initial relative angle of attack resulted in a corresponding reduction in trim values. Furthermore, the trim values with wing sail were smaller than those without wing sail in all cases. These trends were likely to attribute to the influence of the fan, which provided auxiliary propulsion for the wing sail and was positioned toward the bow of the model ship. However, the authors believe that these tendencies would remain consistent under similar operational conditions. Furthermore, the trim values for each condition were presented in Table 8.

On the other hand, the variation of sinkage under various wind conditions was also estimated, as depicted in Fig. 14. However, the sinkage results showed a different trend compared to trim. The results of sinkage exhibited highly irregular patterns regardless of wind speed magnitude and relative angle of attack. The only consistent trend observed was that sinkage values were smaller compared to the baseline condition without wing sail. This could be explained by examining the uncertainty of the LVDT used for sinkage measurement. The uncertainty error of the LVDT employed in the experiment was 0.545 mm, and the current sinkage values of all cases converged within this uncertainty range. Therefore, it was concluded that it would be more accurate to consider these values as having equivalent sinkage. Moreover, the absence of z-directional forces in the wing sail SIL system physically supports the observation of equivalent sinkage values.

Table 8

Trim values under various wind conditions.

Trim angle		Wind angle			
		20°	30°	45°	50°
Wind speed	10 m/s	-0.022 °	-0.023 °	-0.017 °	-0.016 °
	15 m/s	-0.021 °	-0.022 °	-0.013 °	-0.012 °
	20 m/s	-0.017 °	-0.018 °	-0.011 °	-0.006 °
	25 m/s	-0.013 °	-0.014 °	-0.010 °	-0.005 °

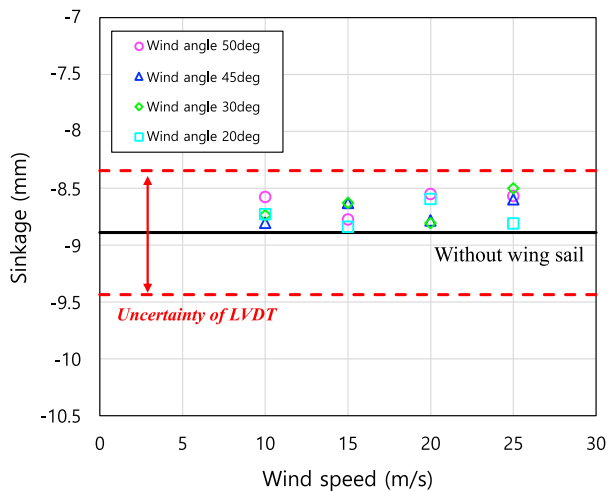


Fig. 14. Variation of sinkage under various wind conditions.

4. Concluding remarks

This study developed a SIL system and applied it to towing tank experiments. Using this system, the changes in drag and motion characteristics of a container ship equipped with wing sails were investigated with a 1:75 scale KCS model equipped with two fans. The SIL system used in the experiments operates through the following process. First, ship motion data with 3-DOF data were acquired from an onboard IMU, and the relative wind velocity vector was computed for each wind condition. From relative wind velocity vector, the relative dynamic angle of attack was obtained, and the resulting total aerodynamic force and moment on the wing sail system were evaluated. These loads were then allocated to the two onboard fans as thrust commands on each axis. This computational cycle was repeated continuously in real-time. Through experiments using this SIL system, the drag reduction effect of the wing sail was measured. As wind speed increased, the resistance reduction rate increased, and it also increased with the initial relative angle of attack. From the ship motion perspective, similar to the drag results, heel angles increased with increasing wind speed and initial relative angle of attack. Quantitatively, the wing sail achieved a maximum resistance reduction of 33%, while the lateral force induced by the wing sail caused a maximum heel angle change of 0.6° . Additionally, trim showed a decreasing trend. However, sinkage exhibited the same results as the case without a wing sail, as there was no downward force acting on the ship. Therefore, at high wind speed an certain angles of attack, wing sails can degrade heel stability and induce large motion variations in container ships depending on loading conditions, so their implementation requires careful consideration.

The contribution of this research can be divided into two parts. The first part involves the application of the SIL method, which has been predominantly employed in FOWT related research, to ship towing tank experiments. Research combining the SIL method with ship towing tank experiments is uncommonly seen, and this work demonstrates the expandability of the SIL methodology to ship related experimental applications. The second aspect involves the assessment of heel variations in container ships caused by wing sails. These results can serve as stability indicators when implementing wing sails on actual container vessels and demonstrate that container loading conditions must also be modified when applying wing sail systems. However, as previously mentioned, several limitations exist in this study due to equipment limitations. The GM of the model ship was intentionally set to a larger value than realistic conditions, and the resistance reduction could not be measured through direct connection with load cells. Therefore, future research is planned to be conducted with these limitations addressed

and improved.

CRediT authorship contribution statement

Gyeongseo Min: Writing – original draft, Validation, Methodology, Investigation, Formal analysis. **Hyeongseok Yoon:** Writing – review & editing, Visualization. **Jaeyoon Jeon:** Writing – review & editing. **Saishuai Dai:** Writing – review & editing. **Sanghyun Kim:** Writing – review & editing. **Daejeong Kim:** Writing – review & editing. **Seungnam Kim:** Writing – review & editing. **Soonseok Song:** Writing – original draft, Project administration, Funding acquisition, Formal analysis, Conceptualization.

Declaration of competing interest

The authors declare that they have no known competing financial interests or personal relationships that could have appeared to influence the work reported in this paper.

Acknowledgements

This research was supported by Korea Institute of Marine Science & Technology Promotion (KIMST) funded by the Ministry of Oceans and Fisheries, Korea (RS-2024-00410200). This work was supported by the Technology Innovation Program (RS-2024-00508368) funded by the Ministry of Trade, Industry & Energy (MOTIE, Korea).

References

- Arnal, V., 2020. *Experimental Modelling of a Floating Wind Turbine Using a «software-in-the-loop» Approach*. École Centrale De Nantes].
- Chen, P., Chen, J., Hu, Z., 2021. Software-in-the-Loop combined reinforcement learning method for dynamic response analysis of FOWTs. *Front. Mar. Sci.* 7. <https://doi.org/10.3389/fmars.2020.628225>.
- Chou, T., Kosmas, V., Acciari, M., Renken, K., 2021. A comeback of wind power in shipping: an economic and operational review on the wind-assisted ship propulsion technology. *Sustainability* 13 (4). <https://doi.org/10.3390/su13041880>.
- Fonseca, N., Soares, C.G., 2012. Experimental study of the performance of a rigid wing sail. *Maritime Eng. Technol.* 45–52.
- Guzelbulut, C., Suzuki, K., 2023. Optimal design of rotor sails based on environmental conditions and cost. *J. Mar. Sci. Eng.* 12 (1). <https://doi.org/10.3390/jmse12010031>.
- Hillenbrand, A., Giovannetti, L.M., Dhomé, U., Kuttenukeuler, J., 2024. Wind tunnel tests of a two-element wingsail with focus on near-stall aerodynamics. *J. Sail. Technol.* 9 (1), 110–127.
- IMO, 2023. *2023 IMO Strategy on Reduction of GHG Emissions from Ships*.
- ITTC, 2014. *General Guideline for Uncertainty Analysis in Resistance Tests*.
- Jiang, X., 2020. *Software-In-The-Loop Applications for Improved Physical Model Tests of Ocean Renewable Energy Devices Using Artificial Intelligence*.
- Kuang, L., Li, H., Su, X., Song, X., Wang, Z., Zhang, Y., Ma, W., 2023. Effect of chord length ratio on aerodynamic performance of two-element wing sail. *Ocean Eng.* 287, 115946.
- Li, C., Wang, H., Sun, P., 2020. Numerical investigation of a two-element wingsail for ship auxiliary propulsion. *J. Mar. Sci. Eng.* 8 (5). <https://doi.org/10.3390/jmse8050333>.
- Ljungberg, E., 2023. *Evaluation of Novel Wingsail Concepts in Terms of Aerodynamic Efficiency*.
- Miller, P., Judge, C., Sewell, D., Williamson, S., 2018. An alternative wing sail concept for small autonomous sailing craft. In: *Robotic Sailing 2017: Proceedings of the 10th International Robotic Sailing Conference*.
- Park, J.Y., Seo, J., Park, D.-W., 2024. Performance evaluation of wing-sail considering the superstructure of the ship. *J. Kor. Soc. Marine Environ. Safety* 30 (7), 896–908. <https://doi.org/10.7837/kosomes.2024.30.7.896>.
- Sauder, T., Alterskjær, S.A., 2022. Hydrodynamic testing of wind-assisted cargo ships using a cyber-physical method. *Ocean Eng.* 243. <https://doi.org/10.1016/j.oceaneng.2021.110206>.
- Silva, M.F., Friebe, A., Malheiro, B., Guedes, P., Ferreira, P., Waller, M., 2019. Rigid wing sailboats: a state of the art survey. *Ocean Eng.* 187. <https://doi.org/10.1016/j.oceaneng.2019.106150>.
- Werner, S., Papanikolaou, A., Werner, S., Fagergren, C., Dessen, L., Kuttenukeuler, J., Santén, V., Steinbach, C., 2023. *The Orcele project—towards wind-powered Ships for Deep Sea Cargo Transport*. SNAME Maritime Convention.
- Wielgosz, C., Dhomé, U., Blackert, E., Giovannetti, L.M., Wallin, S., Kuttenukeule, J., Werner, S., 2025. *The Importance of Scale Effects for Wind Propulsion: Experimental*

and Numerical Analysis of a Wing Sail. SNAME Chesapeake Sailing Yacht Symposium.

Zhu, H., 2020. CFD Investigation of wind-powered Ships Under Extreme Condition: Simulations on the naca-0015 Foil Under Deep Stall Condition.

Zhu, H., Yao, H.-D., Thies, F., Ringsberg, J.W., Ramne, B., 2023. Propulsive performance of a rigid wingsail with crescent-shaped profiles. Ocean Eng. 285. <https://doi.org/10.1016/j.oceaneng.2023.115349>.